



Cite this: DOI: 10.1039/d0nj00523a

Single-pot template-free synthesis of a glycerol-derived C–Si–Zr mesoporous composite catalyst for fuel additive production†

 Saurabh Kumar,^{ab} Nagabhatla Viswanadham,^{ab} Sandeep K. Saxena,^b Arumugam Selvamani,^b Jitendra Diwakar^{ab} and Ala'a H. Al-Muhtaseb^c

Synthesis of a highly ordered mesoporous acid- as well as metal-functionalized carbon (–SO₃H/C–Si–Zr) material is achieved for the first time from a simple single-pot template-free carbonization of low-value bio-derived glycerol. Addition of TEOS to glycerol right before the carbonization was observed to facilitate molecular-level interactions between them to establish C–Si bonding, which eventually leads to the formation of a high surface area mesoporous –SO₃H/C–Si composite material. Unlike this, the addition of ZrO(NO₃)₂·xH₂O to glycerol could not have such an effect, but when Zr is used in the presence of TEOS the mixture could successfully produce the –SO₃H/C–Si–Zr composite possessing mesoporosity and uniform acidity suitable for bulky tri-acetin production useful for fuel applications. Here TEOS is observed to play two roles, (1) as a surface area and porosity improver of graphitic carbon by its C–Si interaction and (2) as a mediator to involve Zr in the carbon composite structure through its Si–OH group. Thus, the combined inclusion of Zr and Si sources in the glycerol-derived carbon structure could successfully introduce the positive aspects of porosity improvement (by Si) and acidity improvement (by zirconia) in the mixed composite –SO₃H/C–Si–Zr to produce the highest ever selectivity of tri-acetin (~94 wt%) from the same low-value bio-derived glycerol by an acetylation reaction. The sustainability of the process lies in the utilization of waste glycerol as a source of the carbon composite, which in turn catalyzes selective low-value glycerol conversion to industrially important fuel additives.

 Received 31st January 2020,
 Accepted 10th April 2020

DOI: 10.1039/d0nj00523a

rsc.li/njc

Introduction

Sustainability and energy conservation aspects of the modern world demand efficient processes for the utilization of low-value carbon feeds as an alternative to fast diminishing fossil sources. Glycerol is one such carbon source with 10 tonnes generated for every 100 tonnes of biodiesel through the *trans*-esterification reaction of fatty acids (vegetable or animal oil) with alcohols.^{1,2} Several catalytic processes using oxides/mixed oxides/zeolite type materials as catalysts have come up to produce various high-value molecules related to fuels and chemicals from crude glycerol.^{2–6} Interestingly, the molecule

glycerol is also a potential candidate for the synthesis of functionalized carbon-based catalysts that in turn can be used for the production of a spectrum of valuable hydrocarbon products.^{7–12} Carbonization of glycerol is a simple method to produce active carbon materials, where sulfonation in the second step creates acid sites for the development of acid-functionalized carbon for catalytic applications.^{13–17} Here carbonization facilitates the formation of a condensed carbon material while the acid-bearing capacity decreases with the severity of carbonization due to the removal of –OH and –COOH groups on the carbonized glycerol.¹⁸ Recently, a novel single-step process for simultaneous carbonization and sulfonation developed in our group has resulted in the creation of highly acid functionalized carbon by –SO₃H interactions with glycerol precursors facilitated at the molecular level, *i.e.*, right from the beginning of the carbonization.¹⁹ Since most reactions require bi-functional catalysts without any molecular level space constraints to facilitate even bulky molecular reactions, the chosen materials should possess important features such as (1) high surface area and mesoporosity, (2) high acid bearing capacity, (3) suitability of the carbon support for metal functionalization depending on the targeted reaction of

^a Academy of Scientific and Innovative Research (AcSIR) at CSIR-Indian Institute of Petroleum, Dehradun 248005, Uttarakhand, India. E-mail: nvish@iip.res.in; Fax: +91-135-2525702; Tel: +91-135-2525856

^b Light Stock Processing Division, Council of Scientific & Industrial Research-Indian Institute of Petroleum, Council of Scientific and Industrial Research, Dehradun 248005, India

^c Department of Petroleum and Chemical Engineering, College of Engineering, Sultan Qaboos University, Muscat 123, Oman

† Electronic supplementary information (ESI) available: Experimental details, SEM, EDX, TEM, XPS *etc.* See DOI: 10.1039/d0nj00523a

interest, (4) high thermal stability and reusability and (5) hydrophilic nature of the material to encourage the adsorption of hydrophilic reactants otherwise difficult to adsorb on lipophilic carbon. Hara *et al.* have done pioneering work on the synthesis of acid functionalized carbon from a variety of bio-mass sources such as starch, cellulose, glucose, *etc.*^{20–22} It was observed that sugar-derived sulfonated amorphous carbon is not suitable for hydrophobic acid-catalysed reactions due to its low surface area, whereas mesoporous silica supported $-\text{SO}_3\text{H}$ bearing sugar-derived amorphous carbon shows significant catalytic performance.²³ However, the synthesis of amorphous carbon materials does not possess features such as high surface area, porosity and hydrophilicity for acid catalysed reactions. These properties can be achieved by the functionalization of heteroatoms (like Si) in the carbon materials and it is highly desirable yet still challenging.^{24–26}

Acetylation of glycerol is one of the most important reactions in the conversion of bio-based low-value glycerol to green bulk chemicals.^{27–32} Here acetylation is expected to occur on three $-\text{OH}$ groups of glycerol (tri-acetin). Depending on the degree of acetylation, the product can be mono-, di- and tri-acetin (Scheme S1, ESI[†]). They have great industrial applications; tri-acetin is widely used in the pharmaceutical, cosmetics, and fuel additive industries, while mono-acetin and di-acetin have been used in the cryogenic industry and as raw materials for biodegradable polyester manufacture.³³ Tri-acetin is easily soluble in biodiesel and has a cetane number improver property, and is thus used as a fuel additive in biodiesel. The blending of biodiesel with 10% tri-acetin leads to the improvement of engine performance in several aspects, such as lower NO_x/CO_x emission along with improved anti-knocking properties.^{34,35} Thus acetylation of glycerol has gained much industrial importance for the production of value-added chemicals having fuel improving properties.^{36,37}

The main challenge involved in the catalyst development for glycerol acetylation is to design the active sites and the porous environment around them to facilitate the bulky molecular reactions of glycerol. A hydrophilic nature of the catalyst surface is also desirable to support the facile adsorption of glycerol and acetic acid for effective catalysis. However, carbonized glycerol has its limitations, especially in terms of surface area, porosity, and the hydrophilic nature. As a way to improve these aspects, composite materials of carbon are chosen in the present study. Silicon from the same group as carbon in the periodic table has been taken for composite preparation. Here the hydroxyl groups associated with silicon are expected to contribute to the desired hydrophilic nature of the catalyst material. Another material chosen for composite preparation is zirconia, as the sulfonation of zirconia is known to create more acidity, required for catalytic applications.^{38–40}

The aim of the present work is to utilize the cheaper carbon source glycerol for the synthesis of a high-quality material that can act as an efficient catalyst to produce high-value fuels and chemicals from glycerol through an acetylation reaction. Here acidic-functionalized, carbonized glycerol mesoporous composite materials such as $-\text{SO}_3\text{H}/\text{C}$, $-\text{SO}_3\text{H}/\text{C}-\text{Si}$, $-\text{SO}_3\text{H}/\text{C}-\text{Zr}$ and

$-\text{SO}_3\text{H}/\text{C}-\text{Si}-\text{Zr}$ have been successfully synthesized *via* a simple single-step carbonization of low-value glycerol (as a carbon source) in the presence of sulfuric acid. The method is expanded for the synthesis of $\text{C}-\text{Si}$, $\text{C}-\text{Zr}$ and $\text{C}-\text{Si}-\text{Zr}$ composite materials, by the simple addition of the corresponding compounds (TEOS for Si and zirconia(IV) oxynitrate for Zr) to glycerol right at the beginning of the carbonization process to establish molecular level interactions of these elements with the carbon precursor.

Herein we report for the first time a facile single-pot method for the synthesis of a $-\text{SO}_3\text{H}/\text{C}-\text{Si}-\text{Zr}$ composite material possessing high surface area, mesopores, high acidity, and thermal stability properties suitable for catalysing bulky molecular reactions. Detailed studies reveal the role of Si as (1) a surface property improver and (2) a mediator element to establish interactions between carbon and zirconia, while Zr contributes to acidity enhancement to make the composite material a promising catalyst for the industrially important glycerol acetylation reaction.

Experimental

Materials

Zirconia(IV) oxynitrate ($\text{ZrO}(\text{NO}_3)_2 \cdot x\text{H}_2\text{O}$, 99.5% pure) was purchased from LOBACHemie Pvt. Ltd. Tetraethyl orthosilicate (TEOS, 98% pure), glycerol (99% pure) and sulfuric acid (98% pure) were purchased from Merck Millipore. All chemicals were used as received without any further purification.

Synthesis of $-\text{SO}_3\text{H}/\text{C}$ and the composite materials

A typical synthesis method involves the preparation of sulfonated carbon by dropwise addition of 60 g of 18 molar conc. sulfuric acid to 20 g of glycerol followed by treatment at 100 °C for 24 h under constant stirring so that dehydration and molecular level interactions between the polar $-\text{SO}_3\text{H}$ group and the carbon moiety occurred. Then the temperature was increased to 180 °C to form a viscous gel. At this stage, N_2 gas was introduced and the temperature is further increased to 300 °C to facilitate the formation of porosity in the $-\text{SO}_3\text{H}$ bearing carbon moiety. The prepared black material is washed thoroughly with an ample amount of boiling water followed by cold water and subsequently calcined in the furnace for 6 h at 500 °C. Similarly, for synthesis of the other three carbon composite ($-\text{SO}_3\text{H}/\text{C}-\text{Si}$, $-\text{SO}_3\text{H}/\text{C}-\text{Zr}$ and $-\text{SO}_3\text{H}/\text{C}-\text{Si}-\text{Zr}$) samples, TEOS, zirconia(IV) oxynitrate and combinations of both (TEOS + zirconia(IV) oxynitrate) were added to the initial glycerol right at the beginning of sulfonation and the carbonization step resulted in the involvement of Si, zirconia, and Si and zirconia in the chemical interaction with the carbon, respectively (a detailed procedure is described in the ESI[†] 1.1–1.2).

Characterization

Scanning Electron Microscopy (SEM, Quanta 200f instrument, Netherlands) and Transmission Electron Microscopy (TEM, Tecnai-12 model, FEI, Netherlands) were used to characterize

the morphology of the samples. X-ray diffraction (XRD) analysis was performed using a D8 Advance, Bruker, Germany, type powder diffractometer with a rotating anode and Cu K α radiation. The scan range was $2\theta = 5\text{--}60^\circ$ with a speed of 2°min^{-1} . FTIR spectra of the samples were recorded with the KBr pellet method on a PerkinElmer-Spectrum Two, USA. Raman spectra were collected using a confocal Raman microscope (XploRA ONE from Horiba) with a 25 mW, 532 nm laser (laser spot size: 2 μm) line from a diode-pumped solid-state laser for excitation. ^{13}C and ^{29}Si NMR spectra of the carbon and Si-containing samples were collected using NMR spectroscopy (Bruker Biospin Switzerland). An Inductively Coupled Plasma Atomic Emission Spectrometer (ICP-AES) (Model: DRE PS 3000UV, M/s Leeman Labs, Inc, USA) was used for elemental analysis. N_2 (77 K) sorption measurements (Micromeritics, ASAP 2010) were conducted to determine the porosity of the samples. The specific surface area (S_{BET}) and pore size distribution were calculated by the volume adsorbed at different P/P_0 values and applying different methods. The total pore volume was calculated by measuring the volume of gas adsorbed at a P/P_0 of 0.99, whereas the t -plot method was used to calculate the micropore surface area (0–20 \AA) using the Harkins–Jura equation. The total micropore volume (0–20 \AA) and the micropore size distribution were obtained by applying the Horvath–Kawazoe method (H–K). X-ray photoemission spectroscopy (XPS, Omicron Nanotechnology, Germany) with monochromatic Al K α radiation ($h\nu = 1486.6 \text{ eV}$) was used to analyse the chemical bonding states of the samples. NH_3 -TPD (Micromeritics Chemisorb 2750 pulse) was used to measure the strength of acidic sites. TGA of the samples was carried out using a Pyris Diamond, PerkinElmer TGA 4000, USA, instrument by heating 2.15 mg samples at $5^\circ \text{C min}^{-1}$ in a flowing air atmosphere.

Results and discussion

The present study aims to explore the synthesis of acid-and metal-functionalized mesoporous carbon composite materials as catalysts for bulky-molecular reactions. Synthesis of Si- and Zr-induced composites with individual as well as simultaneous interactions with the carbon material right from the beginning of acid-functionalization has been studied. Structure–activity relations of the synthesized materials have been discussed.

Properties of the materials

The low angle XRD results of the synthesized $-\text{SO}_3\text{H}/\text{C}$, $-\text{SO}_3\text{H}/\text{C}-\text{Si}$ and $-\text{SO}_3\text{H}/\text{C}-\text{Si}-\text{Zr}$ materials show a sharp diffraction pattern near to $1^\circ 2\theta$ (inset of Fig. 1a, b and d) representing the presence of a mesoporous structure. There is no such diffraction pattern observed in the $-\text{SO}_3\text{H}/\text{C}-\text{Zr}$ sample due to the absence of mesoporosity, which indicates the improper interaction of Zr with carbon. However, when Zr is used in combination with Si, the resultant $-\text{SO}_3\text{H}/\text{C}-\text{Si}-\text{Zr}$ exhibited a low angle XRD peak around $1^\circ 2\theta$. This observation suggests that the presence of Si species facilitated the interaction of zirconia to form a C–Si–Zr mesoporous structure (probably due

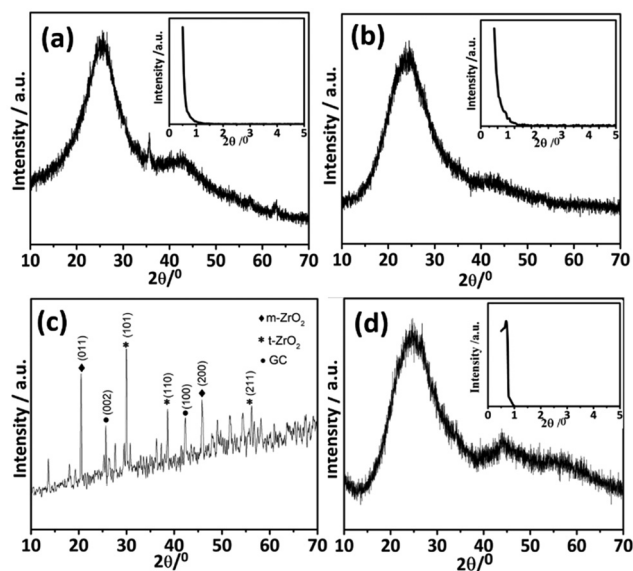


Fig. 1 XRD patterns of samples: (a) $-\text{SO}_3\text{H}/\text{C}$, (b) $-\text{SO}_3\text{H}/\text{C}-\text{Si}$, (c) $-\text{SO}_3\text{H}/\text{C}-\text{Zr}$ and (d) $-\text{SO}_3\text{H}/\text{C}-\text{Si}-\text{Zr}$.

to the hydrophilic nature of Si–OH groups). In wide-angle XRD, all the samples exhibited two prominent diffraction peaks at $2\theta = 25^\circ$ and $2\theta = 43^\circ$ related to the C [002] and C [101] graphitic planes respectively (JCPDS file no. 08-0415).⁴¹ In addition to this, several peaks related to the formation of ZrO_2 have been observed for the C–Zr sample, which again suggests the inferior interaction of Zr with C in this sample.

The FTIR spectrum of $-\text{SO}_3\text{H}/\text{C}$ (Fig. 2a) shows bands at 1715 cm^{-1} , 1598 cm^{-1} , and 1224 cm^{-1} representing the stretching vibrations of C=O and C=C and bending vibration of C–O–C groups respectively, while an intense band at 3420 cm^{-1} is due to the stretching vibrations of –OH groups mainly present in the alcohol and a few carboxylic acid groups. In addition to these, two distinct bands at 1390 cm^{-1} and 1039 cm^{-1} are observed related to symmetric and asymmetric

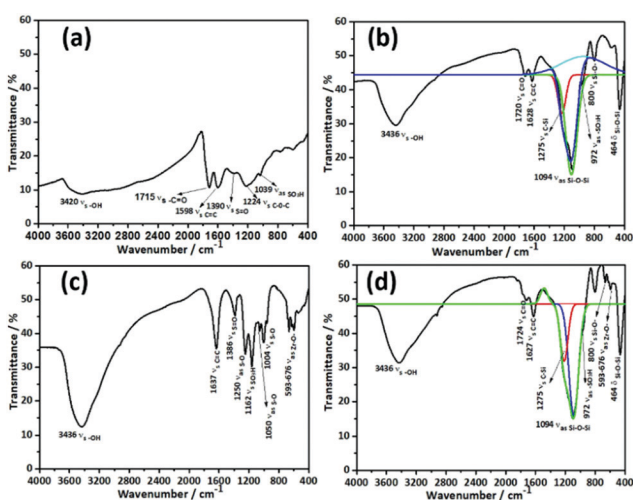


Fig. 2 FTIR spectra of samples: (a) $-\text{SO}_3\text{H}/\text{C}$, (b) $-\text{SO}_3\text{H}/\text{C}-\text{Si}$, (c) $-\text{SO}_3\text{H}/\text{C}-\text{Zr}$ and (d) $-\text{SO}_3\text{H}/\text{C}-\text{Si}-\text{Zr}$.

stretching vibrations of S=O present in $-\text{SO}_3\text{H}$. Overall this result confirms the successful formation of a $-\text{SO}_3\text{H}$, $-\text{COOH}$, and $-\text{OH}$ bearing carbon material by a single-step synthesis route. Introduction of Si during the synthesis resulted in a change in the structural information of the material. As shown in Fig. 2b the material exhibited prominent absorbance bands related to asymmetric and bending mode vibrations of Si–O–Si at 1094 cm^{-1} and 464 cm^{-1} along with a symmetric Si–O band at 800 cm^{-1} .⁴² The deconvoluted spectrum of the Si containing samples showed two additional broad absorbance bands at ~ 1275 and $\sim 1094\text{ cm}^{-1}$ representing C–Si and Si–O–Si vibrations, respectively, as given in Fig. 2. However, the bands related to C=C, C=O and $-\text{SO}_3\text{H}$ groups (1628 , 1720 and 972 cm^{-1}) remain present in the sample, confirming that the $-\text{SO}_3\text{H}/\text{C}$ structure is not disturbed by the additional interaction of Si with C. This sample also shows an enormous increase in the $-\text{OH}$ group concentration that can be ascribed to the presence of the Si–OH group. These observations suggest that the addition of TEOS during the synthesis effectively operated to incorporate Si species into the structure of the sulfonated carbon. For the $-\text{SO}_3\text{H}/\text{C}-\text{Zr}$ sample the FT-IR bands indicate the presence of Zr–O at $593\text{--}676\text{ cm}^{-1}$ (Fig. 2c). Similar to $-\text{SO}_3\text{H}/\text{C}$, the band related to symmetric S=O at 1390 cm^{-1} remains there in the $-\text{SO}_3\text{H}/\text{C}-\text{Zr}$ sample. The formation of four new bands representing sulfonated groups is obtained in this sample. Thus, the zirconia used in the initial glycerol solution is observed to form sulfated zirconia species as an additional source of acidity in the $-\text{SO}_3\text{H}/\text{C}-\text{Zr}$ sample. The presence of Zr also caused a massive increase in the $-\text{OH}$ group concentration observed by the high-intensity band at 3436 cm^{-1} . Finally, the sample prepared by adding both Si and Zr sources to glycerol has shown the presence of C–Si, Si–O–Si and Zr–O bands (Fig. 2d), suggesting a possible interaction of Zr with Si (Si–O–Zr).

^{13}C NMR spectra of the materials show signals at 130, 155, and 188 ppm with spinning sidebands related to polycyclic aromatic carbon atoms, phenolic $-\text{OH}$ bearing carbon and carbonyl carbon of carboxylic acid groups, respectively (Fig. 4).^{43,44} The intensity of the 130 ppm peak related to the polycyclic

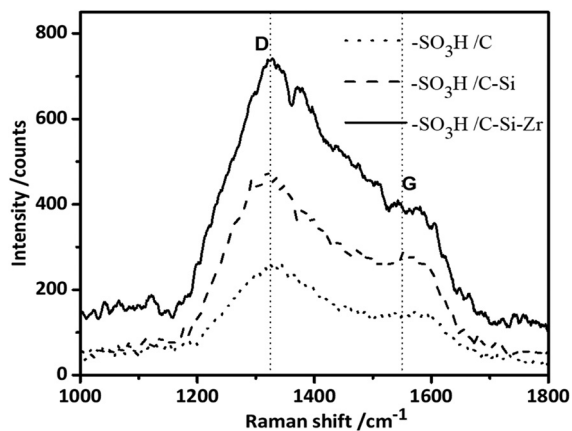


Fig. 3 Raman spectra of samples: (a) $-\text{SO}_3\text{H}/\text{C}$, (b) $-\text{SO}_3\text{H}/\text{C}-\text{Si}$, and (c) $-\text{SO}_3\text{H}/\text{C}-\text{Si}-\text{Zr}$.

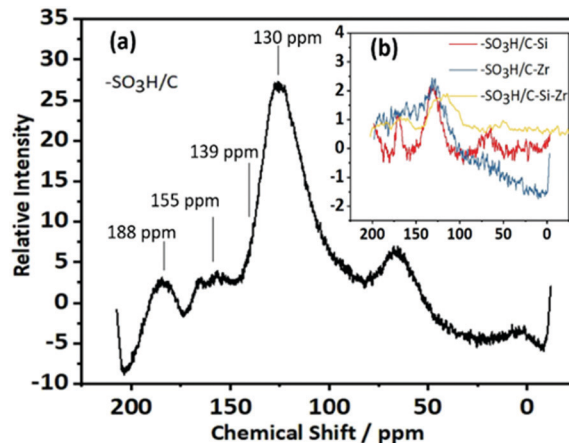


Fig. 4 ^{13}C NMR spectra of samples: (a) $-\text{SO}_3\text{H}/\text{C}$, (b) $-\text{SO}_3\text{H}/\text{C}-\text{Si}$, $-\text{SO}_3\text{H}/\text{C}-\text{Zr}$ and $-\text{SO}_3\text{H}/\text{C}-\text{Si}-\text{Zr}$.

aromatic carbon structure was observed to decrease in the Si-containing $-\text{SO}_3\text{H}/\text{C}-\text{Si}$ and $-\text{SO}_3\text{H}/\text{C}-\text{Si}-\text{Zr}$ samples, which indicates the involvement of Si in the polycyclic-carbon (graphitic) structure. This phenomenon is also supported by the XRD crystallinity of graphitic carbon, which was decreased for the $-\text{SO}_3\text{H}/\text{C}-\text{Si}$ and $-\text{SO}_3\text{H}/\text{C}-\text{Si}-\text{Zr}$ samples (Fig. 1). Further, the G peak intensity in the Raman spectra of the samples also (Fig. 3) indicated a decrease in graphitic carbon formation in the presence of $-\text{SO}_3\text{H}$ groups. Here the samples exhibited two bands, one centered around 1325 cm^{-1} corresponding to the D peak caused by the breathing mode of sp^3 carbon bonds,⁴⁵ and another band around 1550 cm^{-1} corresponding to G originating from sp^2 carbon bond graphitic carbons. The G/D ratio representation of graphitization was observed to decrease in the presence of Si. In addition, small bands at 1244 , 1145 , and 1045 cm^{-1} were also observed, related to the asymmetric vibration of S=O present in the sulfonated carbon samples.

^{29}Si solid-state NMR experiments were carried out to elucidate the chemical environment around Si to confirm the chemical interaction of Si with carbon and zirconia in the samples. Fig. 5 shows the deconvoluted ^{29}Si NMR spectra of the $-\text{SO}_3\text{H}/\text{C}-\text{Si}$ and $-\text{SO}_3\text{H}/\text{C}-\text{Si}-\text{Zr}$ samples, with well-resolved bands at -100 and -110 ppm representing isolated $(-\text{O})_3\text{Si}(\text{OH})$ silanol (Q^3) and siloxane bridges $(-\text{O})_4\text{Si}$ (Q^4) respectively.⁴⁶ The intensity of the Q^4 Si environment is significantly increased in the

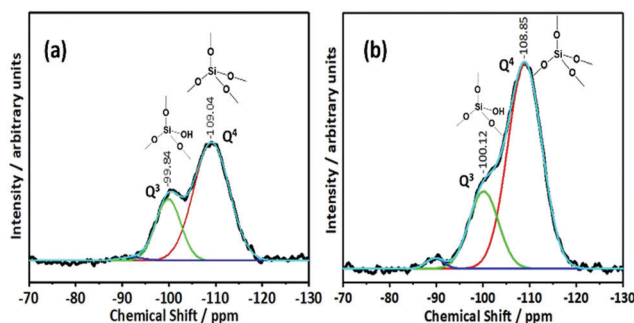


Fig. 5 ^{29}Si NMR spectra of samples: (a) $-\text{SO}_3\text{H}/\text{C}-\text{Si}$ and (b) $-\text{SO}_3\text{H}/\text{C}-\text{Si}-\text{Zr}$.

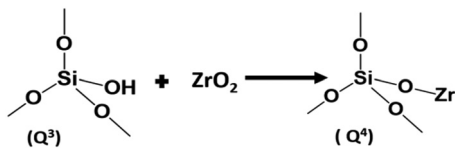


Fig. 6 Efficient interaction of Zr with Si through silanol groups.

$-\text{SO}_3\text{H}/\text{C}-\text{Si}-\text{Zr}$ sample when compared to that of the $-\text{SO}_3\text{H}/\text{C}-\text{Si}$ sample. This can be ascribed to the additional interaction of Q^3 hydroxyl groups with the zirconia species in the former sample, which results in the conversion of some of the Q^3 species into Q^4 , as presented in Fig. 6. This observation suggests that the interaction of Zr with carbon was followed by silanol groups, as evidenced in the FT-IR results.

XPS analysis was adopted to study the surface composition and chemical environment of the synthesized materials. XPS survey spectra show peaks at various binding energy values with respect to $\text{S}2\text{p}$, $\text{O}1\text{s}$, $\text{C}1\text{s}$, $\text{Si}2\text{p}$, $\text{Si}2\text{s}$, and $\text{Zr}3\text{d}$, which indicates the chemical composition of the samples (Fig. S3A, ESI[†]). The chemical environment of all samples was confirmed by $\text{C}1\text{s}$ and $\text{O}1\text{s}$ spectra (Fig. S3B, ESI[†]). The $\text{C}1\text{s}$ spectrum of the $-\text{SO}_3\text{H}/\text{C}$ material shows four peaks attributed to $\text{C}-\text{C}$ at 284 eV, $\text{C}-\text{O}$ at 285 eV, $\text{C}=\text{O}$ at 288 eV, and $\text{O}=\text{C}-\text{O}$ at 290 eV.^{47,48} The presence of Si and Zr in the sulfonated carbon material shows additional peaks at 283 eV and 287 eV characteristic of $\text{Si}-\text{C}$ and $\text{C}-\text{O}-\text{Zr}$, respectively (Fig. S3B, ESI[†]). Here the intensity of the $\text{C}-\text{C}$ peak was decreased by the addition of Si due to the formation of a chemical bond between carbon and Si. The $\text{O}1\text{s}$ spectrum of the $-\text{SO}_3\text{H}/\text{C}$ material (Fig. S3B, ESI[†]) shows three peaks corresponding to oxygen present in various chemical environments; therein the peak centered at 531 eV for oxygen in sulfonated species, 533.37 eV for $\text{C}-\text{OH}/\text{C}-\text{O}$ and 534.84 eV for oxygen in H_2O molecules.⁴⁹ Similarly the $-\text{SO}_3\text{H}/\text{C}-\text{Si}$ and $-\text{SO}_3\text{H}/\text{C}-\text{Si}-\text{Zr}$ materials also showed three peaks with respect to the same oxygen environments, but there is a decrease in the intensity of oxygen in sulfonyl groups and an increase in the intensity of oxygen in H_2O molecules. This can be ascribed to the dilution in sulfonated species associated with the carbon material caused by the presence of Si and Zr in the composite materials. The peak related to oxygen in H_2O was ascribed to chemisorbed water associated with the samples, whose concentration depends on the hydrophilic nature of the samples. The intensity of this peak is increased in the Si and Zr containing samples. The presence of Si and or zirconia is also expected to influence the change in the overall charge on the

surface reflected in the shifting of the peak positions towards higher B.E. in these samples. The shifting of the $-\text{SO}_3\text{H}$ peak is highest in the case of the $-\text{SO}_3\text{H}/\text{C}-\text{Si}-\text{Zr}$ sample to higher B.E., and this almost merged with that of $\text{C}-\text{O}$. Overall the FTIR, Raman, ^{13}C NMR, ^{29}Si NMR and XPS data support the formation of $-\text{SO}_3\text{H}/\text{C}$ by the effective interaction of $\text{C}-\text{Si}$ in the Si-containing samples and interaction of Si and Zr in the $-\text{SO}_3\text{H}/\text{C}-\text{Si}-\text{Zr}$ sample.

The surface area data indicate that there is a negligible surface area ($2\text{ m}^2\text{ g}^{-1}$) created in the $-\text{SO}_3\text{H}/\text{C}$ sample. Whereas, the introduction of Si (TEOS) significantly improved this property and the resultant $-\text{SO}_3\text{H}/\text{C}-\text{Si}$ sample exhibited a $379\text{ m}^2\text{ g}^{-1}$ surface area (Table 1). In N_2 adsorption-desorption experiments, the $-\text{SO}_3\text{H}/\text{C}$ sample exhibits a type IV isotherm with a prominent loop configuration between 0.4 and 1.0 P/P_0 corresponding to the filling of mesopores (Fig. 7b). The combined addition of Si and zirconia compounds during sulfonation of carbon shows an interesting influence on the design of ordered-mesoporosity in the $-\text{SO}_3\text{H}/\text{C}-\text{Si}-\text{Zr}$ sample, which exhibits a sharp adsorption loop at $\sim 0.7 P/P_0$. It is also reflected in the higher surface area ($\sim 253\text{ m}^2\text{ g}^{-1}$) of the $-\text{SO}_3\text{H}/\text{C}-\text{Si}-\text{Zr}$ sample. The concept of enhanced porosity and pore size order of the $-\text{SO}_3\text{H}/\text{C}-\text{Si}-\text{Zr}$ sample can be analyzed using the BJH pore size distribution curves shown in Fig. 7a. Although both the $-\text{SO}_3\text{H}/\text{C}-\text{Si}$ and $-\text{SO}_3\text{H}/\text{C}-\text{Si}-\text{Zr}$ samples exhibit mesopores up to 20 nm, the mesopores in the range of $\sim 10\text{ nm}$ increased significantly in the latter sample. This can be ascribed to the ordering in mesopore size formation of the Si and Zr containing carbon samples. Here, the presence of Si seems to be responsible for mesopore creation. As given in Table 1, the carbon samples involving Si possessed significant pore volume contributed by mesopores ($0.448\text{ cm}^3\text{ g}^{-1}$ and $0.496\text{ cm}^3\text{ g}^{-1}$ in the case of the $-\text{SO}_3\text{H}/\text{C}-\text{Si}$ and $-\text{SO}_3\text{H}/\text{C}-\text{Si}-\text{Zr}$ sample respectively), compared to the corresponding Si-free samples. The increase in the surface area and porosity of the Si-containing materials is due to the creation of $\text{C}-\text{Si}$ arrangements in polycyclic graphitic carbon, which leads to a change in the carbon environment, which was clearly observed from Raman and ^{13}C -NMR analyses.

Table 1 clearly elucidates the NH_3 -TPD results of the synthesized samples; it was observed that $-\text{SO}_3\text{H}/\text{C}$ exhibits two types of acidity, namely weak and strong with a value of 1.84 and 15.70 mmol g^{-1} respectively. The presence of a high value of strong acidity (15.70 mmol g^{-1}) is possibly due to the desorption of lots of $-\text{SO}_3\text{H}$ groups occurring at a temperature of above $400\text{ }^\circ\text{C}$ as evidenced from DT/TGA. However, the

Table 1 Physico-chemical properties of the samples

| Sl. no. | Sample | Acidity ^a (mmol g^{-1}) | | Si ^b (At. wt%) | Zr ^b (At. wt%) | S_{BET}^c ($\text{m}^2\text{ g}^{-1}$) | $t\text{-plot}^c S_{\text{Micro}}$ ($\text{m}^2\text{ g}^{-1}$) | $t\text{-plot}^c S_{\text{Exter}}$ ($\text{m}^2\text{ g}^{-1}$) | Median ^c pore width (nm) | V_{Total}^c ($\text{cm}^3\text{ g}^{-1}$) | $t\text{-plot}^c$ | |
|---------|---|---|--------|------------------------------|------------------------------|--|--|--|--|---|--------------------|-------------------|
| | | Weak | Strong | | | | | | | | V_{Micro} | V_{Meso} |
| 1 | $-\text{SO}_3\text{H}/\text{C}$ | 1.84 | 15.70 | — | — | 2 | 4.26 | 1.90 | 1.22 | 0.002 | 0.002 | 0.000 |
| 2 | $-\text{SO}_3\text{H}/\text{C}-\text{Si}$ | 2.47 | 1.75 | 18.78 | — | 378 | 63.23 | 315.75 | 5.30 | 0.480 | 0.032 | 0.448 |
| 3 | $-\text{SO}_3\text{H}/\text{C}-\text{Zr}$ | 2.54 | 4.21 | — | 7.86 | 5 | 2.94 | 1.91 | 3.25 | 0.009 | 0.001 | 0.008 |
| 4 | $-\text{SO}_3\text{H}/\text{C}-\text{Si}-\text{Zr}$ | 0.56 | 6.54 | 17.58 | 5.32 | 253 | 35.68 | 217.17 | 11.74 | 0.514 | 0.018 | 0.496 |

^a Measured by NH_3 -TPD. ^b Obtained by ICP-AES analysis. ^c Obtained by BET study.

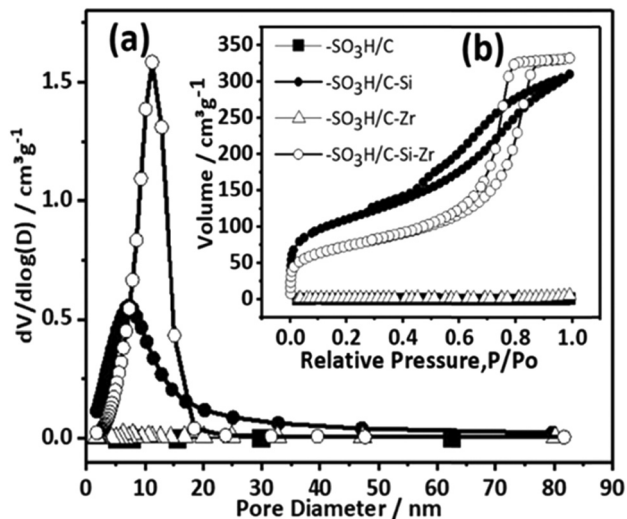


Fig. 7 (a) BJH pore size distribution curve and (b) N_2 adsorption-desorption isotherms of samples: $-SO_3H/C$, $-SO_3H/C-Si$, $-SO_3H/C-Zr$ and $-SO_3H/C-Si-Zr$.

$-SO_3H/C-Si$ sample shows lower acidity compared to $-SO_3H/C$ due to the dilution effect caused by the proportional amount of Si, which cannot contribute anything to the acidity. Here the mere role of Si is to have a dilution effect on the acidic sites created by sulfonated carbon. Unlike Si, the addition of zirconia provides additional $-SO_3H/Zr$ sites.^{42,50,51} Hence, in the sample $-SO_3H/C-Zr$, both carbon and zirconia are the source sites for the sulfonate group interaction. Simultaneous addition of Si and Zr precursors during sulfonation of glycerol created $-SO_3H/C-Si-Zr$, where again Si acts as an acid-diluting agent, while sulfonated carbon and zirconia are the sources of acidic sites. This sample exhibited a broad distribution of acidic sites.

The SEM image of the $-SO_3H/C$ material indicates a sheet morphology (Fig. S1a, ESI[†]), while the $-SO_3H/C-Si$, $-SO_3H/C-Zr$ and $-SO_3H/C-Si-Zr$ samples show particles with a sheet-like morphology (Fig. S1b–d, ESI[†]). The SEM-EDX results indicate the concentrations of the constituent elements carbon, silicon, zirconium, sulfur and oxygen present in the synthesized materials (Fig. S1, ESI[†]). A significant increase in the S content was also observed in the case of the Zr containing composite materials (when compared to the sulfonated C sample), due to the presence of additional S present in the form of sulfonated zirconia species in these samples. The atomic weight% of Si and Zr elements is also analyzed by ICP-AES analysis. The data reveal the chemical involvement of Si, Zr and $-SO_3H$ species in the structures of the respective samples during their synthesis (Table 1). Further, the morphology and particle size of the materials were confirmed with the help of TEM analysis (Fig. S2a–h, ESI[†]), which confirms the presence of a hexagonal morphology (5–10 nm). The presence of lattice fringes in the TEM images represents the ordered crystalline nature of the samples.

The DT/TGA analysis of the samples given in Fig. S4, ESI[†] shows an endothermic weight loss below 150 °C related to the removal of moisture and adsorbed water on all the samples.¹⁹ Above this temperature, the weight loss is mainly due to the

decomposition of $-SO_3H$ groups observed above 400 °C in all the samples except $-SO_3H/C-Zr$. In the $-SO_3H/C-Zr$ sample, the corresponding peak was observed at 600 °C, suggesting relatively higher thermal stability of the sample.

Confirmation of the C–Si interaction during carbonization and sulfonation of glycerol

There is direct evidence for C–Si interactions obtained from the XPS spectrum of C1s of the $-SO_3H/C-Si$ material (Fig. S3B, ESI[†]), where a peak at B.E ~ 284.69 eV corresponding to C–Si was observed.⁵² In addition to this, ^{13}C NMR and XRD also provided indirect evidence for C–Si interactions. It is well known that carbon compounds get polymerized during carbonization to give a graphitic structure. In XRD the intensity of the band at $2\theta = 43^\circ$ representing the C[101] plane of graphitic carbon has been decreased in the Si-containing catalyst when compared to the $-SO_3H/C$ catalyst (Fig. 1) due to the possible reason of involvement of Si in the carbon structure to decrease the graphitic carbon formation to an extent. Similarly, in ^{13}C NMR, the peak at 130 ppm with respect to polycyclic aromatic carbons was drastically decreased by the addition of Si (Fig. 4), which indicates Si–C interactions as the reason for the decrease in the polymerized carbon structure. However, in IR, the C–Si band at 1275 cm^{-1} is not clearly distinguished due to its merging with the high-intensity dominant band of Si–O–Si in the Si-containing catalyst (Fig. 2). The graphitic nature of the carbonized carbon in the catalysts has been identified from Raman spectra (Fig. 3). In the Si-containing samples, the intensity of the G peak representing graphitic carbon is decreased with a simultaneous increase in the D peak, which also supports the graphitic interaction of Si as the reason for the decrease in the G peak intensity. Overall, the results clearly suggest that Si is successfully involved in the structure of the sulfonated carbon during carbonization to give the $-SO_3H/C-Si$ structure. Detailed studies indicated a significant improvement in the properties of the carbonized materials in the presence of Si. A steep increase in the surface area properties was observed in the $-SO_3H/C-Si$ catalyst; prominent loop formation in the N_2 adsorption–desorption isotherm (Fig. 7b) and the formation of 10 nm mesopores measured in BJH pore size measurements were seen, which are collectively reflected in a huge increase in the surface area from 2 to $379\text{ m}^2\text{ g}^{-1}$ in the C–Si catalyst (Table 1). This catalyst also possesses a $0.480\text{ cm}^3\text{ g}^{-1}$ pore volume contributed mainly by mesopore creation facilitated by the Si interaction with the carbon in the catalyst. The NH_3 -TPD results are also clear evidence of the C–S interaction, where $-SO_3H/C$ exhibits higher acidity than $-SO_3H/C-Si$ due to the dilution effect of Si leading to a decrease in the number of $-SO_3H$ groups in the carbon. In contrast the $-SO_3H/C-Zr$ sample shows increased acidity due to the greater interaction of $-SO_3H$ with Zr as well as carbon. Thus, combined addition of Si and Zr in $-SO_3H/C$ exhibits more acidity compared to that of the other samples.

Interaction of zirconia with carbon (in the presence and absence of Si) during carbonization and sulfonation of glycerol

From the material characterization results, no clear-cut evidence was observed to prove the interaction of zirconia with carbon in

the $-\text{SO}_3\text{H}/\text{C}-\text{Zr}$ catalyst. Further, the XRD pattern shows the presence of prominent bands related to ZrO_2 in the sample, which suggests a poor or no interaction of zirconia with carbon. Unlike Si, the presence of zirconia could not contribute to the increase in the surface area and porosity properties, while these values are almost similar to those of the carbon alone catalyst (Table 1). This will further support the lack of Zr participation in the carbon structure to modify its properties. In NH_3 -TPD, a broad range of acidity was observed, perhaps due to the formation of some sulfonated zirconia acid sites in this catalyst. Since the interaction of Si with carbon is confirmed and contributed to significant enhancement in the surface area properties in the C-Si sample, a combination of Si and Zr along with C is studied in the $-\text{SO}_3\text{H}/\text{C}-\text{Si}-\text{Zr}$ sample. The efforts made to establish the zirconia interaction with carbon in the presence of the Si source as a facilitator indeed resulted in the successful creation of the $-\text{SO}_3\text{H}/\text{C}-\text{Si}-\text{Zr}$ composite material. In the XRD patterns of $-\text{SO}_3\text{H}/\text{C}-\text{Si}-\text{Zr}$, no ZrO_2 pattern representing the individual identity of zirconia was observed. Thus, the ZrO_2 formation which is obvious in the $-\text{SO}_3\text{H}/\text{C}-\text{Zr}$ catalyst has been restricted in the presence of Si due to the possible reason of molecular-level interactions of zirconia facilitated by the C-Si structure of $-\text{SO}_3\text{H}/\text{C}-\text{Si}-\text{Zr}$ in this sample. This can be ascribed to the role of Si as a mediator to facilitate such C-Zr interactions in the structure. The efficient interaction of Zr with Si through the silanol group is confirmed from ^{29}Si NMR spectra, which is reflected in the conversion of Q^3 species of Si into Q^4 upon Zr loading (Fig. 6). Here, the $-\text{OH}$ groups on Si are expected to facilitate the interaction with zirconia to involve Zr in the structure of $-\text{SO}_3\text{H}/\text{C}-\text{Si}-\text{Zr}$. The easy interaction of Si species with carbon on one hand and zirconia species on the other may be due to the catenation property/small atomic size and hydrophilic nature of Si species respectively. This interaction is expected to give enhanced material properties such as high surface area and porosity with the presence of the Si source (Fig. 8), which is supported and confirmed by the characterization data. It is interesting to see that the poor porosity possessing $-\text{SO}_3\text{H}/\text{C}-\text{Zr}$ catalyst exhibits a significant improvement in porosity upon the introduction of Si ($-\text{SO}_3\text{H}/\text{C}-\text{Si}-\text{Zr}$). Hence, the role of Si may be ascribed to its two functions: (1) as a surface area and porosity improver of graphitic carbon and (2) as a mediator to facilitate interactions between C and Zr. Thus, by the combined inclusion of zirconia and Si, we could successfully introduce the positive aspects of porosity improvement (by Si) and acidity improvement (by zirconia) in the mixed composite $-\text{SO}_3\text{H}/\text{C}-\text{Si}-\text{Zr}$ material.



Fig. 8 Schematic illustration of the effect of Si involvement in the enhancement of the surface area/porosity of carbon composite materials.

Reaction studies

Glycerol acetylation is an acid-catalysed reaction that requires acid sites with sufficient strength along with molecular level space around (surface area and pore size) the active sites for facilitating the formation of bulky reaction products (Scheme S1, ESI†). The reaction has industrial importance due to the product applications, especially di- and tri-acetin whose selectivity is greatly influenced by the strength of the acid sites and the space available around the active sites. Hence, sufficient acidity, surface area, and porosity are three essential material properties required for its efficient catalytic activity towards this reaction. Acid functionalized carbon materials have inferior properties in terms of lower surface area, porosity and acidity. As a way to improve these properties, in the present work, Si is introduced to improve the surface area/porosity properties, while zirconia for acidity improvement, through the single-pot carbonization of a glycerol, TEOS and $\text{ZrO}(\text{NO}_3)_2 \cdot x\text{H}_2\text{O}$ mixture for their effective molecular level interaction right from the beginning of the active site construction in the carbon-based composite materials. The performance of the resultant materials was tested towards the glycerol acetylation reaction. The performances of the acid-functionalized carbon and carbon composite materials as catalysts towards the glycerol acetylation reaction under the best conditions are given in Table 2. It was observed that all the catalysts exhibited $\sim 95\%$ conversion of glycerol, indicating the efficiency of the synthesized materials towards catalytic activity. A blank run is also conducted (following the same reaction conditions in the absence of any catalyst) to ascertain the catalytic role of the materials. Table 2 (Sl. No. 1) clearly shows that the conversion of glycerol was very low (15%) in the absence of a catalyst, where the selectivity of mono-acetin and di-acetin was found to be higher but tri-acetin was zero. These observations are clearly suggesting that the $-\text{SO}_3\text{H}/\text{C}-\text{Si}-\text{Zr}$ catalyst plays an important role in the effective conversion of glycerol into the tri-acetin molecule due to its suitable acidity and ordered mesoporous structure. Though all the catalysts exhibited comparable conversions, the selectivity towards various products has been observed to vary depending on the catalyst and reaction parameters, as discussed in the following section.

Effect of reaction temperature

The reaction temperature does not have an effect on the conversion but on the product selectivity. As in the case

Table 2 Glycerol conversion and product selectivity over sulfonated carbon and carbon composite catalysts

| Sl. No. | Catalysts | Conv. of glycerol (%) | Selectivity (%) | | |
|---------|---|-----------------------|-----------------|------|------|
| | | | MA | DA | TA |
| 1 | Blank run | 15 | 83.3 | 13.7 | — |
| 2 | $-\text{SO}_3\text{H}/\text{C}$ | 100 | 97.6 | 2.4 | — |
| 3 | $-\text{SO}_3\text{H}/\text{C}-\text{Si}$ | 100 | 5.7 | 94.3 | — |
| 4 | $-\text{SO}_3\text{H}/\text{C}-\text{Zr}$ | 99.5 | 4.1 | 70.3 | 25.6 |
| 5 | $-\text{SO}_3\text{H}/\text{C}-\text{Si}-\text{Zr}$ | 97 | 3.1 | — | 93.9 |

Reaction conditions: reaction temperature – 150°C , reaction time – 5 h, wt. of catalyst – 100 mg and feed mole ratio (glycerol:AcOH) – 1 : 9

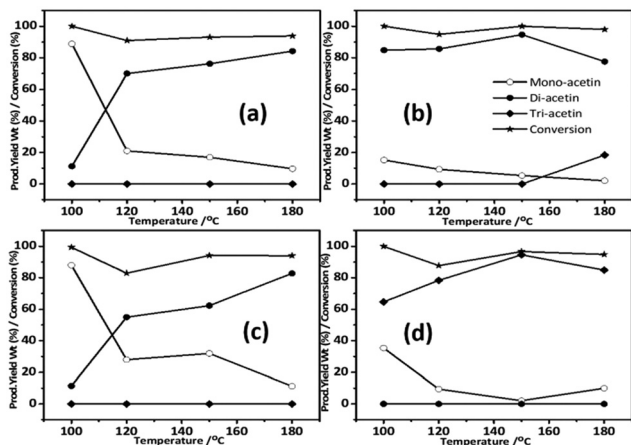


Fig. 9 Effect of reaction temperature over (a) $-\text{SO}_3\text{H}/\text{C}$, (b) $-\text{SO}_3\text{H}/\text{C}-\text{Si}$, (c) $-\text{SO}_3\text{H}/\text{C}-\text{Zr}$ and (d) $-\text{SO}_3\text{H}/\text{C}-\text{Si}-\text{Zr}$. Reaction conditions: reaction temperature – 150 to 180 °C, reaction time – 5 h, wt. of catalyst – 100 mg and feed mole ratio (glycerol : AcOH) – 1 : 9.

of $-\text{SO}_3\text{H}/\text{C}$ (Fig. 9a), increasing temperature enhanced the selectivity towards di-acetin with a simultaneous decrease of mono-acetin, suggesting the bi-functional esterification progressed with reaction severity. But for the $-\text{SO}_3\text{H}/\text{C}-\text{Si}$ catalyst (Fig. 9b) the selectivity to di-acetin is prominent even at 150 °C, and the reaction temperature does not cause any measurable enhancement in its selectivity, except the formation of tri-acetin, which is observed at 180 °C. The superior performance in terms of di-acetin and tri-acetin selectivity of this catalyst cannot be ascribed to the acidity, because the presence of Si caused dilution of acid sites but not an increase in acidity (Table 1). Here, two catalyst properties, namely surface area and porosity are improved by the addition of Si (Fig. 7 and Table 1). These surface properties and the space availability in the pores possibly influence the bulky molecule formation. Thus, the higher di-acetin formation and appearance of tri-acetin for the $-\text{SO}_3\text{H}/\text{C}-\text{Si}$ composite can be ascribed to positive aspects of both acidity and porosity, where the extra acidity is created by sulfonated zirconia and the higher porosity is created by Si in this catalyst. Thus, the $-\text{SO}_3\text{H}/\text{C}-\text{Si}-\text{Zr}$ catalyst produced higher tri-acetin along with some di-acetin at 150 °C (Fig. 9d). At higher reaction temperatures (150 to 180 °C), a slight decrease in tri-acetin formation with simultaneous formation of di-acetin was observed, which indicates the de-acetylation reaction. Overall, the results suggest the positive role of the acidity and porosity aspects of the $-\text{SO}_3\text{H}/\text{C}-\text{Si}-\text{Zr}$ catalyst in the product selectivity in the glycerol acetylation reaction.

Effect of reaction time

The reaction time does not show much influence on the glycerol conversion as almost 80% conversion is achieved in the first one hour, which is increased to near 100% in the second hour of the reaction time (Fig. 10), but the selectivity to the products was changed with time. In the case of $-\text{SO}_3\text{H}/\text{C}$, the selectivity to mono-acetin is dominant at the initial reaction time, which shifted to di-acetin after 5 h reaction time. This observation suggests the formation of di-acetin through

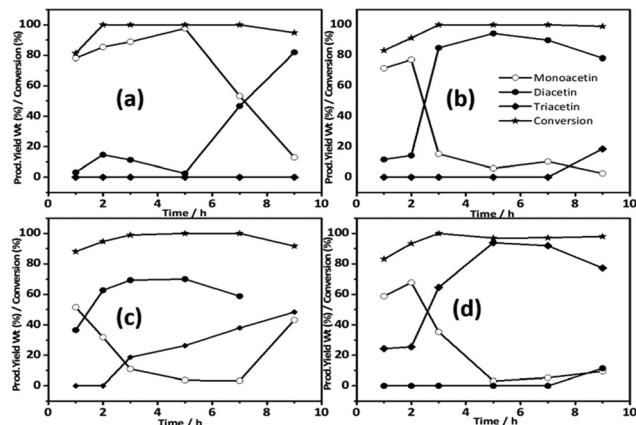


Fig. 10 Effect of reaction time over (a) $-\text{SO}_3\text{H}/\text{C}$, (b) $-\text{SO}_3\text{H}/\text{C}-\text{Si}$, (c) $-\text{SO}_3\text{H}/\text{C}-\text{Zr}$ and (d) $-\text{SO}_3\text{H}/\text{C}-\text{Si}-\text{Zr}$. Reaction conditions: reaction temperature – 150 °C, reaction time – 1 to 9 h, wt. of catalyst – 100 mg and feed mole ratio (glycerol : AcOH) – 1 : 9.

the mono-acetin intermediate. Even after extended hours of reaction time, tri-acetin formation does not occur on this catalyst. A similar trend is observed for the $-\text{SO}_3\text{H}/\text{C}-\text{Si}$ based catalyst also, but the formation of di-acetin is attained quickly within 3 h reaction time on this catalyst (Fig. 10b). On this catalyst, tri-acetin formation was also observed but after longer reaction hours. Different from those, the $-\text{SO}_3\text{H}/\text{C}-\text{Si}-\text{Zr}$ catalyst exhibited tri- and di-acetin formation at the initial reaction time itself (Fig. 10d). The selectivity to tri-acetin is continuously increased up to 5 h reaction time to a selectivity as high as 93.8% tri-acetin. The absence of mono-acetin and high selectivity of tri-acetin on $-\text{SO}_3\text{H}/\text{C}-\text{Si}-\text{Zr}$ reveals the positive role of acidity and porosity contributed by zirconia and Si on this catalyst as a responsible factor for bulky product formation. The acidity analysis of the fresh and spent catalysts also supports the stable performance of the $-\text{SO}_3\text{H}/\text{C}-\text{Si}-\text{Zr}$ catalyst. Fig. 11 shows the NH_3 -TPD acidity patterns of fresh and spent catalysts, where the fresh catalysts of $-\text{SO}_3\text{H}/\text{C}$, $-\text{SO}_3\text{H}/\text{C}-\text{Si}$ and $-\text{SO}_3\text{H}/\text{C}-\text{Zr}$ exhibit high acidity but the acidity declined significantly on the corresponding spent catalyst (Fig. 11a–c). On the other hand, for $-\text{SO}_3\text{H}/\text{C}-\text{Si}-\text{Zr}$ the acid sites are observed to mostly remain on the spent catalysts (Fig. 11d).

Possible reason for the superior performance of the $-\text{SO}_3\text{H}/\text{C}-\text{Si}-\text{Zr}$ catalyst

In the case of $-\text{SO}_3\text{H}/\text{C}$, though the acidity is high, the fact that the catalyst exhibited inferior selectivity to tri-acetin can be ascribed to its negligible surface area and porosity (Table 1). The catalyst also took a long reaction time to produce di-acetin. The relatively higher hydrophobic nature of the carbon not suitable for reactant affinity is also responsible for its inferior product selectivity. The $-\text{SO}_3\text{H}$ groups attached to hydrophobic carbon also exhibited inferior stability as reflected in the NH_3 -TPD analysis of the spent catalysts (Fig. 11). Introduction of Si in the $-\text{SO}_3\text{H}/\text{C}-\text{Si}$ composite improved the creation of significant porosity in the catalyst as revealed by the N_2 adsorption-desorption isotherm and surface area values (Fig. 7

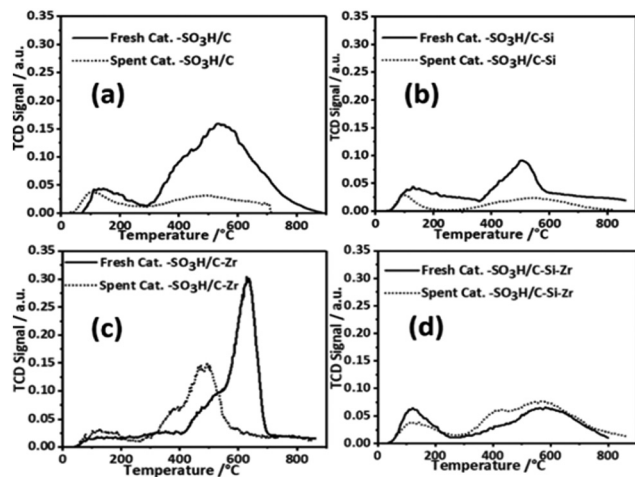


Fig. 11 NH_3 -TPD profiles of fresh and spent catalysts: (a) $-\text{SO}_3\text{H}/\text{C}$, (b) $-\text{SO}_3\text{H}/\text{C}-\text{Si}$, (c) $-\text{SO}_3\text{H}/\text{C}-\text{Zr}$ and (d) $-\text{SO}_3\text{H}/\text{C}-\text{Si}-\text{Zr}$.

and Table 1). This catalyst also exhibited higher di-acetin formation and even tri-acetin at higher reaction temperatures (Table 2). It is interesting to see that the acidity of the $-\text{SO}_3\text{H}/\text{C}-\text{Si}$ catalyst is lower than the $-\text{SO}_3\text{H}/\text{C}$ alone catalyst due to the dilution of sulfonated carbon sites by Si (Table 1). In spite of the lower acidity, the superior performance of $-\text{SO}_3\text{H}/\text{C}-\text{Si}$ especially for bulky molecule formation can be ascribed to its surface area and porosity. The composite of $-\text{SO}_3\text{H}/\text{C}-\text{Zr}$ resulted in different types of behaviour. Though the acidity property is improved by sulfonation at both carbon and zirconia sites, the porosity was not improved in this catalyst. Hence the catalyst exhibited an intermediate behaviour between $-\text{SO}_3\text{H}/\text{C}$ and $-\text{SO}_3\text{H}/\text{C}-\text{Si}$ in catalytic activity. In an attempt to get positive aspects of porosity improvement of Si and acidity improvement of zirconia, the mixed composite $-\text{SO}_3\text{H}/\text{C}-\text{Si}-\text{Zr}$ prepared in the study indeed resulted in the creation of significant porosity and acidity in the catalyst. The catalyst also exhibited a good hydrophilic nature as revealed by FT-IR (Fig. 2), which is required for the efficient adsorption of polar reactant molecules in the esterification reaction. Due to this reason, we have achieved very high tri-acetin selectivity on this catalyst even at the initial reaction time, and the catalyst also sustained its active sites against leaching supported by comparable product yields analysed up to several reactions runs (Table 2), and comparable acidity patterns recorded for the spent catalyst (Fig. 11). In the absence of Si, the catalysts $-\text{SO}_3\text{H}/\text{C}$ and $-\text{SO}_3\text{H}/\text{C}-\text{Zr}$ exhibited inferior hydrophilicity and the $-\text{SO}_3\text{H}$ groups associated with these materials provide inferior stability against deactivation (leaching) as revealed from spent catalysts analysis (Fig. 11). Overall, the improvement in the surface area, porosity, dilution of the acid site density and hydrophilic nature of the $-\text{SO}_3\text{H}/\text{C}-\text{Si}-\text{Zr}$ catalyst seems to be responsible for its superior catalytic performance in the bulky-molecular glycerol esterification reaction. The present study provides simultaneous carbonization sulfonation involving heteroatom incorporation (Si/Zr) as a novel, simple and single-step technique to prepare acid-functionalized mesoporous carbon composite materials possessing suitable acidity and

sustainability for bulky molecular catalytic applications. The performance of the synthesized catalyst of the present study was observed to be promising like other catalyst materials such as zeolites, mesoporous materials, resins, composite materials, and functionalized carbon catalysts reported so far (Table S1, ESI[†]). The present catalyst system also exhibited superior catalytic activity towards tri-acetin with a yield of about 93.8 wt%, which is the highest ever reported to the best of our knowledge.

Conclusions

The present work demonstrates a template-free method for the synthesis of Si and Zr containing, $-\text{SO}_3\text{H}$ bearing mesoporous carbon composite materials by a simple single-pot simultaneous carbonization and sulfonation of glycerol in the presence of TEOS and $\text{ZrO}(\text{NO}_3)_2$. The interaction of Si with the carbon source resulted in controlled carbonization by the formation of C-Si bonds in the $-\text{SO}_3\text{H}/\text{C}-\text{Si}$ material, possessing a more than 100 fold increase in surface area contributed by 10–20 nm size pores suitable for bulky molecular catalytic applications. However, in the absence of the Si source, the interaction between Zr and C could not be established effectively to cause any enhancement in such surface properties. But the presence of zirconia can be a source for additional $-\text{SO}_3\text{H}$ sites. The positive aspects of both Si and Zr can be successfully introduced in the preparation of the $-\text{SO}_3\text{H}/\text{C}-\text{Si}-\text{Zr}$ material. By virtue of the enhanced catalytic properties, the $-\text{SO}_3\text{H}/\text{C}-\text{Si}-\text{Zr}$ material possessed excellent catalytic activity toward the acetylation of glycerol reaction for the production of bulky molecular tri-acetin (~ 94 wt%) at higher glycerol conversion ($\sim 97\%$). The material also exhibited excellent reproducibility and reusability determined from reaction data and spent catalyst characterization studies. The composite material synthesized by sulfonation of bio-derived waste-glycerol as a carbon source for catalyst preparation, which in turn converts waste-glycerol to produce industrially important fuel-additive tri-acetin, provides an economic and green method for waste utilization. The catalyst material also can be applied for other acid-catalyzed bulky molecular reactions. The simple single-pot synthesis method developed for functionalized carbon composites of the present study can be expanded for the incorporation of other suitable elements (other than Si and Zr) in the periodic table for vivid applications.

Conflicts of interest

There are no conflicts to declare.

Acknowledgements

S. K. is thankful to the director, CSIR-IIP Dehradun and AcSIR for his enrollment in doctoral program. S. K. thanks DST (AORC) INSPIRE, INDIA for awarding an INSPIRE fellowship. We are thankful to the XRD, IR, NMR, SEM and TEM analysis groups at IIP for analysis.

Notes and references

- M. H. Haider, N. F. Dummer, D. W. Knight, R. L. Jenkins, M. Howard, J. Moulijn, S. H. Taylor and G. J. Hutchings, *Nat. Chem.*, 2015, **7**, 1028–1032.
- L. Faba, E. Díaz and S. Ordóñez, *Renewable Sustainable Energy Rev.*, 2015, **51**, 273–287.
- M. Morales, P. Y. Dapsens, I. Giovinazzo, J. Witte, C. Mondelli, S. Papadokostantakis, K. Hungerbühler and J. Pérez-Ramírez, *Energy Environ. Sci.*, 2015, **8**, 558–567.
- D. Cespi, F. Passarini, G. Mastragostino, I. Vassura, S. Larocca, A. Iaconi, A. Chiericato, J. L. Dubois and F. Cavani, *Green Chem.*, 2015, **17**, 343–355.
- Z. Wu, H. Yan, S. Ge, J. Gao, T. Dou, Y. Li, A. C. K. Yip and M. Zhang, *Catal. Commun.*, 2017, **92**, 80–85.
- G. M. Lari, G. Pastore, M. Haus, Y. Ding, S. Papadokostantakis, C. Mondelli and J. Pérez-Ramírez, *Energy Environ. Sci.*, 2018, **11**, 1012–1029.
- E. Lam and J. H. T. Luong, *ACS Catal.*, 2014, **4**, 3393–3410.
- D. Sun, Y. Yamada, S. Sato and W. Ueda, *Green Chem.*, 2017, **19**, 3186–3213.
- N. Gupta, O. Khavryuchenko, A. Villa and D. Su, *ChemSusChem*, 2017, **10**, 3030–3034.
- K. Shen, X. Chen, J. Chen and Y. Li, *ACS Catal.*, 2016, **6**, 5887–5903.
- X. Cao, S. Sun and R. Sun, *RSC Adv.*, 2017, **7**, 48793–48805.
- S. H. Y. S. Abdullah, N. H. M. Hanapi, A. Azid, R. Umar, H. Juahir, H. Khatoun and A. Endut, *Renewable Sustainable Energy Rev.*, 2017, **70**, 1040–1051.
- A. V. Nakhate and G. D. Yadav, *ACS Sustainable Chem. Eng.*, 2016, **4**, 1963–1973.
- L. J. Konwar, P. Mäki-Arvela, A. J. Thakur, N. Kumar and J. P. Mikkola, *RSC Adv.*, 2016, **6**, 8829–8837.
- J. Howard, D. W. Rackemann, J. P. Bartley, C. Samori and W. O. S. Doherty, *ACS Sustainable Chem. Eng.*, 2018, **6**, 4531–4538.
- R. M. N. Kalla, M.-R. Kim and I. Kim, *Ind. Eng. Chem. Res.*, 2018, **57**, 11583–11591.
- S. De, A. M. Balu, J. C. van Der Waal and R. Luque, *ChemCatChem*, 2015, **7**, 1608–1629.
- D. W. Lee, M. H. Jin, J. C. Park, C. B. Lee, D. Oh, S. W. Lee, J. W. Park and J. S. Park, *Sci. Rep.*, 2015, **5**, 1–11.
- N. Viswanadham, S. Debnath, S. K. Saxena and A. H. Al-Muhtaseb, *RSC Adv.*, 2016, **6**, 41364–41368.
- K. Nakajima and M. Hara, *ACS Catal.*, 2012, **2**, 1296–1304.
- S. Saganuma, K. Nakajima, M. Kitano, D. Yamaguchi, H. Kato, S. Hayashi and M. Hara, *J. Am. Chem. Soc.*, 2008, **130**, 12787–12793.
- K. Fukuhara, K. Nakajima, M. Kitano and S. Hayashi, *ChemCatChem*, 2015, 3945–3950.
- K. Nakajima, M. Okamura, J. N. Kondo, K. Domen, T. Tatsumi, S. Hayashi and M. Hara, *Chem. Mater.*, 2009, **21**, 186–193.
- J. Liu, N. P. Wickramaratne, S. Z. Qiao and M. Jaroniec, *Nat. Mater.*, 2015, **14**, 763–774.
- W. Qi, C. He, Q. Wang, S. Liu, Q. Yu, W. Wang, N. Leksawasdi, C. Wang and Z. Yuan, *ACS Sustainable Chem. Eng.*, 2018, **6**, 3640–3648.
- D. S. Su, G. Wen, S. Wu, F. Peng and R. Schlögl, *Angew. Chem., Int. Ed.*, 2017, **56**, 936–964.
- U. Chandrakala, R. B. N. Prasad and B. L. A. Prabhavathi Devi, *Ind. Eng. Chem. Res.*, 2014, **53**, 16164–16169.
- P. S. Kong, M. K. Aroua, W. M. A. W. Daud, H. V. Lee, P. Cognet and Y. Pérès, *RSC Adv.*, 2016, **6**, 68885–68905.
- J. R. Dodson, T. d. C. M. Leite, N. S. Pontes, B. Peres Pinto and C. J. A. Mota, *ChemSusChem*, 2014, **7**, 2728–2734.
- Shagufta, I. Ahmad and R. Dhar, *Catal. Surv. Asia*, 2017, **21**, 53–69.
- C. De La Calle, J. M. Fraile, E. García-Bordejé, E. Pires and L. Roldán, *Catal. Sci. Technol.*, 2015, **5**, 2897–2903.
- R. Calmanti, M. Galvan, E. Amadio, A. Perosa and M. Selva, *ACS Sustainable Chem. Eng.*, 2018, **6**, 3964–3973.
- J. I. García, H. García-Marín and E. Pires, *Green Chem.*, 2014, **16**, 1007–1033.
- A. Cornejo, I. Barrio, M. Campoy, J. Lázaro and B. Navarrete, *Renewable Sustainable Energy Rev.*, 2017, **79**, 1400–1413.
- R. C. Elias, M. Senra and L. Soh, *Energy Fuels*, 2016, **30**, 7400–7409.
- P. U. Okoye, A. Z. Abdullah and B. H. Hameed, *Fuel*, 2017, **209**, 538–544.
- R. Jothi Ramalingam, T. Radhika, F. Adam and T. H. Dolla, *Int. J. Ind. Chem.*, 2016, **7**, 187–194.
- M. M. Hosseini, E. Kolvari, N. Koukabi, M. Ziyaei and M. A. Zolfogol, *Catal. Lett.*, 2016, **146**, 1040–1049.
- M. S. Tiwari, A. B. Gawade and G. D. Yadav, *Green Chem.*, 2017, **19**, 963–976.
- Y. Zhang, Q. Xiong, Y. Chen, M. Liu, P. Jin, Y. Yan and J. Pan, *Ind. Eng. Chem. Res.*, 2018, **57**, 1968–1979.
- D. Gupta, S. Kundu and B. Saha, *RSC Adv.*, 2016, **6**, 100417–100426.
- M. A. F. e Santos, I. P. Lôbo and R. S. da Cruz, *Mater. Res.*, 2014, **17**, 700–707.
- T. Jiang, V. L. Budarin, P. S. Shuttleworth, G. Ellis, C. M. A. Parlett, K. Wilson, D. J. Macquarrie and A. J. Hunt, *J. Mater. Chem. A*, 2015, **3**, 14148–14156.
- D. Lee, *Molecules*, 2013, **18**, 8168–8180.
- T. Cai, W. F. Qiu, D. Liu, W. J. Han, L. Ye, A. J. Zhao and T. Zhao, *J. Chem. Soc., Dalton Trans.*, 2013, **42**, 4285–4290.
- P. Krasucka, J. Goworek and A. Kierys, *Adsorption*, 2016, **22**, 663–671.
- Y. Wei, X. Ling, L. Zou, D. Lai, H. Lu and Y. Xu, *Colloids Surf., A*, 2015, **482**, 507–513.
- P. A. Russo, M. M. Antunes, P. Neves, P. V. Wiper, E. Fazio, F. Neri, F. Barreca, L. Mafra, M. Pillinger, N. Pinna and A. A. Valente, *Green Chem.*, 2014, **16**, 4292–4305.
- Q. Guan, Y. Li, Y. Chen, Y. Shi, J. Gu, B. Li, R. Miao, Q. Chen and P. Ning, *RSC Adv.*, 2017, **7**, 7250–7258.
- H. Gao, Y. Peng, J. Pan, J. Zeng, C. Song, Y. Zhang, Y. Yan and W. Shi, *RSC Adv.*, 2014, **4**, 43029–43038.
- B. L. Oliveira and V. Teixeira Da Silva, *Catal. Today*, 2014, **234**, 257–263.
- S. Zeng, W. Feng, S. Peng, Z. Teng, C. Chen, H. Zhang and S. Peng, *RSC Adv.*, 2019, **9**, 30685–30692.